2020 IEEE International Conference on Robotics and Automation (ICRA)
31 May - 31 August, 2020. Paris, France

Aortic 3D Deformation Reconstruction using 2D X-ray Fluoroscopy and 3D Pre-operative Data for Endovascular Interventions

Yanhao Zhang[1], Liang Zhao[1(✉)], and Shoudong Huang[1]

***Abstract*— Current clinical endovascular interventions rely on 2D guidance for catheter manipulation. Although an aortic 3D surface is available from the pre-operative CT/MRI imaging, it cannot be used directly as a 3D intra-operative guidance since the vessel will deform during the procedure. This paper aims to reconstruct the live 3D aortic deformation by fusing the static 3D model from the pre-operative data and the 2D live imaging from fluoroscopy. In contrast to some existing deformation reconstruction frameworks which require 3D observations such as RGB-D or stereo images, fluoroscopy only presents 2D information. In the proposed framework, a 2D-3D registration is performed and the reconstruction process is formulated as a non-linear optimization problem based on the deformation graph approach. Detailed simulations and phantom experiments are conducted and the result demonstrates the reconstruction accuracy and robustness, as well as the potential clinical value of this framework.**

***Index Terms*— aortic deformation reconstruction, fluoroscopy, endovascular interventions.**

I. Introduction

The application of endovascular interventions has broadened the options for treating cardiovascular diseases [1] [2] [3]. However, such interventions are still challenging tasks for surgeons to precisely manipulate catheters via a fragile and complex endovascular system in an environment with physiological movements [4] [5] [6]. Although the robotic systems have been applied for facilitating catheter operations, they usually rely on 2D guidance from intra-operative X-ray fluoroscopy for 3D operations [7] [8]. On the other hand, an aortic 3D shape can be acquired pre-operatively through medical imaging approaches such as computed tomography (CT) scans. Hence, one way for achieving 3D guidance is to intra-operatively overlay this pre-operative model with fluoroscopy. However, because of the dynamic nature of the vasculature, the pre-operative shape is insufficient to represent aortic deformation, and therefore the deformation should be updated intra-operatively [9].

In the field of minimal invasive surgery (MIS), there have been some works considering the 3D reconstruction from an existing 3D model using multiple intra-operative 2D X-ray images. However, many of them focus on the recovery of bones [10] [11] [12], which have much fewer deformations compared with that of the vasculature. Currently, there are few works focussing on the recovery of aortic deformation using intra-operative X-ray images. An as-rigid-as-possible method is used in [13] to correct the distortion of intra-operative overlay, but it requires the position of the inserted endovascular catheter.

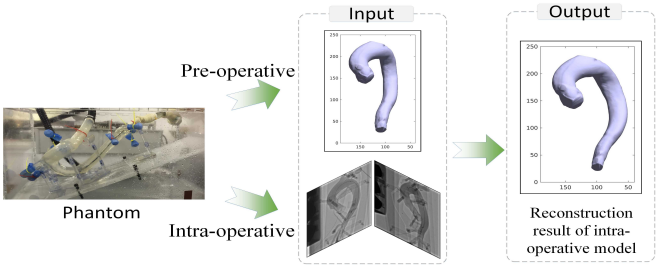

Fig. 1. Input & output of the proposed deformation reconstruction problem.

On the other hand, as an extension of the simultaneous localization and mapping (SLAM) problem, dynamically recovering the 3D shape of a deformable object has been studied in different scenarios. DynamicFusion [14] extends KinectFusion [15] and proposes a 3D reconstruction framework for deformable object observed by an RGB-D sensor. The non-rigid warp field is parametrized using dual quaternions [16]. This framework is then improved in [17] [18] [19], and has been extended for stereoscope localization and mapping in MIS [20] where the warp field is parametrized using embedded deformation (ED) graph [21] and the surface texture is considered for surgical environments.

In this paper, a framework for robustly recovering aortic 3D deformation is proposed using a vessel's pre-operative 3D model and multiple intra-operative X-ray images (Fig. 1). Different from the above works where the depth information along the optical axis is observed by an RGB-D or stereo camera, radiographic fluoroscopy (with orthographic projection) only provides a 2D observation. The unavailability of the depth information and the occlusion of overlying structures (Fig. 2b) limit the methods used in the previous works to be applied in this scenario.

In order to deal with the limitation of orthographic projection and reduce the influence of partial occlusions on X-ray fluoroscopy, in this paper, pixels which present the aortic wall contours are selected as the observed features. A 2D-3D registration approach is applied to calculate correspondence according to these features. The vessel's reconstruction is formulated as a nonlinear optimization problem based on the ED graph approach. Detailed validation using simulations and phantom experiments are performed to evaluate the accuracy of the reconstruction result and the robustness to observation noises. Both simulations and phantom experi-

[1]Yanhao Zhang, Liang Zhao, and Shoudong Huang are with Centre for Autonomous Systems, Faculty of Engineering and Information Technology, University of Technology Sydney, Ultimo, New South Wales, NSW 2007, Australia (e-mails: Yanhao.Zhang@student.uts.edu.au; Liang.Zhao@uts.edu.au; Shoudong.Huang@uts.edu.au). This work is supported by Australian Research Council (ARC) Discovery Project DP200100982.

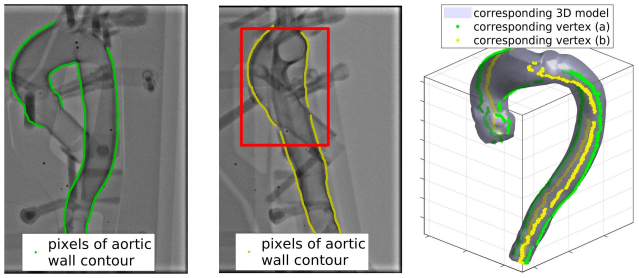

(a) (b) (c)

Fig. 2. An example illustrating the X-ray fluoroscopy and the 3D model. The first two figures present the X-ray images viewing the same deformed 3D vessel model from different directions, where green and yellow colour represent the pixels used as the observed features. The last figure presents the corresponding 3D model and the corresponding vertices of the features.

ments illustrate the reconstruction ability (with average error around 0.7mm-0.8mm for simulations and 0.9mm-1.2mm for phantom experiments) using only two intra-operative X-ray images. This shows the potential clinical value of the proposed framework to be applied for endovascular interventions using X-ray angiography system, e.g. G-arm or biplane angiography system.

II. Problem Description

This paper aims to develop a method to reconstruct the live 3D aortic shape for catheter guidance. The proposed framework combines the pre-operative 3D model and the intra-operative fluoroscopy observations such that the 3D vessel model is reconstructed intra-operatively. Fig. 1 outlines the input and output of the proposed reconstruction problem.

Let $\mathcal{M}$ represent the shape of the pre-operative mesh model consisting of a number of vertices whose positions are denoted as $\{\mathbf{P}_1, \cdots, \mathbf{P}_N\}$. The objective is to estimate its intra-operative shape with deformation, $\widehat{\mathcal{M}}$ (the new positions of all vertices), based on multiple X-ray images, e.g. two images I_1, I_2 of the same deformed model obtained from two different directions (Fig. 2a and Fig. 2b). The pixels presenting the aortic wall contours $\mathbf{p}_{l_i}$ (l denotes the image index while i denotes the index of the pixel in image I_l) are selected as the observed features.

The projection model of an orthographic image is:

$$\mathbf{p} = s\mathbf{U}\mathbf{R}(\mathbf{P} + \mathbf{t}) + \boldsymbol{\epsilon}, \tag{1}$$

where $\mathbf{P} \in \mathbb{R}^3$ represents the $[x, y, z]$ coordinates of a 3D vertex from the deformed model, $\mathbf{p} \in \mathbb{R}^2$ represents the 2D pixel of this point. s is a scale factor representing the inverse of pixel space which means the actual length (in millimetres) between two pixels. $\mathbf{R}$, $\mathbf{t}$ represent the relative pose from model frame to image frame. $\mathbf{U} = \begin{bmatrix}\mathbf{I}_2, \mathbf{0}_{2\times 1}\end{bmatrix}$ is for getting the two upper rows of the full rotation matrix $\mathbf{R}$, and $\boldsymbol{\epsilon} \in \mathbb{R}^2 \sim \mathcal{N}(\mathbf{0}, \boldsymbol{\Sigma})$ represents the noise that corrupts observation. The two main difficulties of using X-ray fluoroscopy in the 3D reconstruction are shown in Fig. 2. i) Fig. 2b illustrates that the phantom model is obscured by part of its own structure from this viewing direction. ii) Due to the orthographic projection, the depth (distance along camera's optical axis) of the 3D corresponding vertices (Fig. 2c) is unknown from the X-ray fluoroscopy.

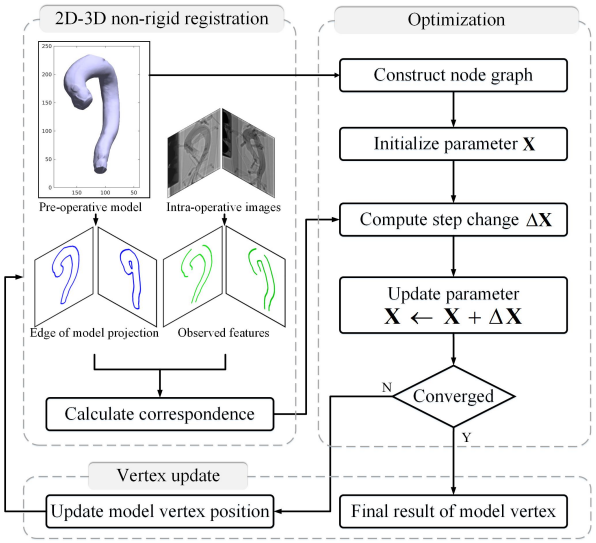

Fig. 3. A flowchart showing the main processes of the proposed deformation reconstruction framework.

III. Methodology

The proposed reconstruction framework consists of three parts: 2D-3D non-rigid registration, parameters estimation, and model vertices update (Fig. 3).

A. 2D-3D non-rigid registration

This process is for calculating the corresponding vertices from aortic model according to observation from X-ray fluoroscopy. To increase the robustness of partial occlusions, pixels that present vessel wall contours (Fig. 2a and Fig. 2b) are used as the features for 2D-3D registration.

To find the corresponding 3D vertex from pre-operative model to each feature, we first project all vertices into image frame according to orthographic projection (1) to get a 2D point cloud. We then calculate the edge of this point cloud via the alpha-shape method with proper alpha radius [22].

In this way, we simplify the 2D-3D registration problem to a 2D-2D registration problem. The basic idea of the 2D non-rigid registration is similar to the iterative closest point (ICP) algorithm [23]. Because of the non-rigidity, the projection of the pre-operative model is different from what is observed on X-ray images, therefore only using Euclidean distance to perform registration increases the chance of wrong matching. To improve the matching quality, we also consider geometric information, normal vectors, when calculating correspondence.

Let $\mathcal{P}^{\text{ob}} = \{\mathbf{p}_1^{\text{ob}}, \cdots, \mathbf{p}_{N^{\text{ob}}}^{\text{ob}}\}$ represent the features (pixels) from an X-ray image, $\mathcal{P}^{\text{md}} = \{\mathbf{p}_1^{\text{md}}, \cdots, \mathbf{p}_{N^{\text{md}}}^{\text{md}}\}$ and $\widetilde{\mathcal{P}}^{\text{md}} = \{\mathbf{P}_1^{\text{md}}, \cdots, \mathbf{P}_{N^{\text{md}}}^{\text{md}}\}$ represent the edge points of model projection in 2D image frame and 3D model frame, $\mathbf{p}_i^{\text{ob}} \in \mathbb{R}^2$ ($i = 1, \cdots, N^{\text{ob}}$), $\mathbf{p}_j^{\text{md}} \in \mathbb{R}^2$, $\mathbf{P}_j^{\text{md}} \in \mathbb{R}^3$ ($j = 1, \cdots, N^{\text{md}}$). For each $\mathbf{p}_i^{\text{ob}}$, we first calculate the set of potential corresponding points $\mathcal{P}_i \subset \mathcal{P}^{\text{md}}$ according to following rule:

$$\begin{aligned}\mathcal{P}_i = \{\mathbf{p}_j^{\text{md}} \,|\, & \mathbf{p}_j^{\text{md}} \in \mathcal{P}^{\text{md}}, \\ & d(\mathbf{p}_i^{\text{ob}}, \mathbf{p}_j^{\text{md}}) < d_{\text{th}},\ \theta(\mathbf{n}(\mathbf{p}_i^{\text{ob}}), \mathbf{n}(\mathbf{p}_j^{\text{md}})) < \theta_{\text{th}}\},\end{aligned} \tag{2}$$

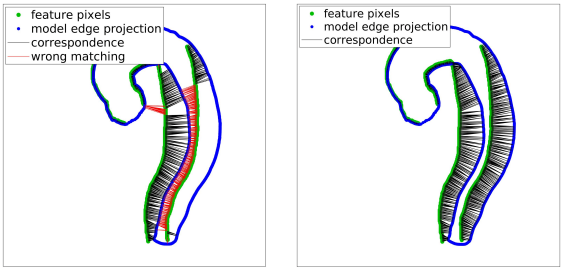

(a) Without geometric information (b) With geometric information

Fig. 4. An illustration of improvement on matching result using geometric information. Green points: feature pixels from fluoroscopy, blue points: edge points of model projection, black lines: correct matching result, red lines: wrong matching using pure Euclidean distance.

where $\mathbf{n}(\cdot) \in \mathbb{R}^2$ denotes the 2D normal vector in image frame, $d(\cdot)$ represents Euclidean distance between two points, $\theta(\cdot)$ represents the angle between two normal vectors. d_{th} and θ_{th} are distance and angle threshold. If $\mathcal{P}_i = \emptyset$, we skip this feature, otherwise, the 2D corresponding points w.r.t. $\mathbf{p}_i^{\text{ob}}$ is calculated by:

$$\tilde{\mathbf{p}}_i^{\text{md}} = \underset{\mathbf{p}_j^{\text{md}} \in \mathcal{P}_i}{\arg\min}\, d(\mathbf{p}_i^{\text{ob}}, \mathbf{p}_j^{\text{md}}). \tag{3}$$

Therefore, the 3D corresponding point from $\widetilde{\mathcal{P}}^{\text{md}}$ is obtained, denoted as $\tilde{\mathbf{P}}_i^{\text{md}}$ [1]. Fig. 4 shows the improvement of matching result using geometric information in our algorithm.

It is noted that for improving reconstruction performance, we recalculate 2D-3D registration in each iteration during the optimization (Section III-D). More details are shown in Algorithm 1.

B. Deformation reconstruction

This framework employs ED graph to reconstruct intra-operative aortic shape according to registration result. ED graph was first proposed in [21]. Its main idea is to use the weighted average of local affine transformations to represents the whole deformation. The deformation graph consists of a set of uniformly scattered sparse graph nodes whose positions $\mathbf{g}_j \in \mathbb{R}^3$ are usually calculated by down-sampling the model vertices [20]. The local transformation around each ED node can be calculated using an affine matrix $\mathbf{A}_j \in \mathbb{R}^{3\times3}$ and a translation vector $\mathbf{t}_j \in \mathbb{R}^3$. For any vertex $\mathbf{P}_i$ from a 3D model, its new position after deformation is calculated using its K nearest ED nodes:

$$\begin{aligned} \hat{\mathbf{P}}_i &= \sum_{j=1}^{K} w_j(\mathbf{P}_i)\left[\mathbf{A}_j\left(\mathbf{P}_i - \mathbf{g}_j\right) + \mathbf{g}_j + \mathbf{t}_j\right], \\ w_j(\mathbf{P}_i) &= \left(1 - \|\mathbf{P}_i - \mathbf{g}_j\|/d_j\right)/n_j, \end{aligned} \tag{4}$$

where weight $w_j(\mathbf{P}_i)$ is used for quantifying the influence of ED node j to vertex i, d_j is the distance to the $K+1$ nearest ED node, and n_j is the normalization factor.

[1]For simplicity, the rest of this paper will ignore superscript 'ob' and 'md' when the meaning is clear from the context.

C. Energy function

According to the registration result, ED graph estimates the deformation parameters (affine matrices and translation vectors) by minimizing the energy function:

$$E = w_{\text{rot}}E_{\text{rot}} + w_{\text{reg}}E_{\text{reg}} + w_{\text{ob}}E_{\text{ob}}. \tag{5}$$

This energy function has three components: rotation term, regularization term, and observation term.

The rotation term is for making the affine matrices close to rotations. E_{rot} is the sum of all rotation error:

$$\begin{aligned} E_{\text{rot}} &= \sum_{j=1}^{M} \text{Rot}(\mathbf{A}_j), \\ \text{Rot}(\mathbf{A}_j) &= (\mathbf{c}_1^\top \mathbf{c}_2)^2 + (\mathbf{c}_1^\top \mathbf{c}_3)^2 + (\mathbf{c}_2^\top \mathbf{c}_3)^2 \\ &\quad + (\mathbf{c}_1^\top \mathbf{c}_1 - 1)^2 + (\mathbf{c}_2^\top \mathbf{c}_2 - 1)^2 + (\mathbf{c}_3^\top \mathbf{c}_3 - 1)^2, \end{aligned} \tag{6}$$

where $\mathbf{c}_1$, $\mathbf{c}_2$, and $\mathbf{c}_3$ are the column vectors of each affine matrix $\mathbf{A}_j$, and M is the number of ED nodes.

The regularization term is for smoothing the deformation and preventing divergence of the neighbouring nodes. The basic idea is that the effect of an ED node and its neighbouring nodes should be almost the same on the overlapping part. E_{reg} is the sum of squared distance errors of this condition:

$$E_{\text{reg}} = \sum_{j=1}^{M} \sum_{i \in \mathbb{N}(j)} \alpha_{ji} \|\mathbf{A}_j\left(\mathbf{g}_i - \mathbf{g}_j\right) + \mathbf{g}_j + \mathbf{t}_j - \left(\mathbf{g}_i + \mathbf{t}_i\right)\|^2, \tag{7}$$

where $\mathbb{N}(j)$ is the index set of neighbouring nodes w.r.t. node j. Weight α_{ji} reflects the degree to which the influence of nodes j and i overlap. This paper follows [21] and sets $\alpha_{ji} = 1$ for all nodes.

The observation term is for penalizing the misalignment between the reconstruction result and the observation. Distance between pair-wise corresponding points generated by the 2D-3D registration described in Section III-A is used for the measurement. Assuming for image I_l, a feature and its corresponding point from the 3D model are $\{\mathbf{p}_{l_i}, \tilde{\mathbf{P}}_{l_i}\}$, then the observation term is the sum of squared distance between all corresponding points

$$E_{\text{ob}} = \sum_{l=1}^{L} \sum_{i \in \mathbb{N}(l)} \|s\mathbf{U}\mathbf{R}_l(\hat{\mathbf{P}}_{l_i} + \mathbf{t}_l) - \mathbf{p}_{l_i}\|^2_{\mathbf{\Sigma}_{l_i}^{-1}}, \tag{8}$$

where $\hat{\mathbf{P}}_{li}$ is calculated by $\tilde{\mathbf{P}}_{l_i}$ using (4), $\mathbb{N}(l)$ is the index set of pair-wise points with correspondence in this image, L is the total number of intra-operative X-ray images. Please note that the observation term is different from the back-projection approach in [18] [24] [20] where depth information is available.

D. Optimization

The estimate of deformation parameters for minimizing E in (5) can be processed using an iterative approach similar to Gauss-Newton algorithm. Here we rewrite the affine matrices and translation vectors to a concatenation vector $\mathbf{X}$ and use $\mathbf{f}(\mathbf{X})$ to denote the residuals of the energy function,

Algorithm 1: Aortic deformation reconstruction

Input: Features from different images, pixel space, poses of image frames, pre-operative 3D model.
Output: 3D deformation reconstruction of aortic model.

Down sample vertices to construct node graph;
Project model vertex onto each image by (1);
while *Algorithm not converged* **do**
  Step 1: 2D-3D registration:
  Calculate the edge of the projections;
  Calculate normal vectors of all points in $\mathcal{P}^{\text{ob}}$, $\mathcal{P}^{\text{md}}$;
  while *loop over each image* **do**
    while *loop over each feature from* $\mathcal{P}^{ob}$ **do**
      Calculate corresponding points by (2), (3);
    end
  end
  Step 2: Optimization:
  Initialize parameter vector $\mathbf{X}$;
  Calculate residuals $\mathbf{f}(\mathbf{X})$ and its Jacobian $\mathbf{J}(\mathbf{X})$;
  Calculate step change $\Delta\mathbf{X}$;
  if $F(\mathbf{X}+\Delta\mathbf{X}) < F(\mathbf{X})$ **then**
    Update parameter vector $\mathbf{X} \leftarrow \mathbf{X}+\Delta\mathbf{X}$;
  else
    Process line search for damping factor α;
    Update parameter vector $\mathbf{X} \leftarrow \mathbf{X}+\alpha\Delta\mathbf{X}$;
  end
  Step 3: Vertex update:
  Update the position of vertices by (4);
  Project the updated vertex onto each image by (1).
end

namely $E := F(\mathbf{X}) = \mathbf{f}(\mathbf{X})^\top \mathbf{f}(\mathbf{X})$. Then the estimation of parameter vector $\mathbf{X}$ is a non-linear least squares problem.

In each iteration, the solver linearizes the problem at current $\mathbf{X}$ to calculate the step change $\Delta\mathbf{X}$ and update $\mathbf{X}$. Let $\mathbf{J}(\mathbf{X})$ represent the Jacobian of $\mathbf{f}(\mathbf{X})$, $\Delta\mathbf{X}$ is obtained by solving

$$(\mathbf{J}^\top\mathbf{J})\Delta\mathbf{X} + \mathbf{J}^\top\mathbf{f} = \mathbf{0}. \tag{9}$$

If the updated energy is lower than before $F(\mathbf{X}+\Delta\mathbf{X}) < F(\mathbf{X})$, we accept the step change ($\mathbf{X} \leftarrow \mathbf{X}+\Delta\mathbf{X}$). Otherwise, for better convergence performance, we use a line search method [25]. The basic idea is to iteratively search a damping factor to the step change so that the energy function $F(\mathbf{X}+\alpha\Delta\mathbf{X})$ decreases relative to $F(\mathbf{X})$. The position of each vertex is updated using the new $\mathbf{X}$ by (4). This updated mesh model $\mathcal{M}'$ is then projected onto the image to calculate a new 2D-3D registration for the next iteration. More details are shown in Algorithm 1.

It is noted that a single image is unable to provide constraints on full 3D direction because of orthographic projection. This has been shown in Fig. 2 that depth information is not observable from orthographic fluoroscopy, which means the deformation of the aortic pre-operative model along depth direction is not observable. However, when multiple images with different viewing angles are used, though depth observation is still unavailable on each image, the regularization term helps to share constraints from different directions, and therefore a full 3D deformation constraints can be achieved. This is indicated by the fact that the Hessian matrix $\mathbf{J}^\top\mathbf{J}$ is of full rank.

IV. Experiments and results

The proposed reconstruction framework was validated by simulations and phantom experiments. Using simulations, reconstruction accuracy was first assessed via three different datasets, and reconstruction robustness was then evaluated via Monte Carlo experiments with multi-level noises. Afterwards, phantom experiments with three datasets were performed. Both simulations and phantom experiments illustrate the capability of our framework for recovering the deformation when using only two intra-operative images from proper viewing directions. For phantom experiments, the 3D reconstruction error is around 0.9mm-1.2mm, decreases around 80%-90% w.r.t. the initial difference between pre-operative model and ground truth.

A. Experimental setup

1) Phantom setup: A Silicone aortic phantom (Materialise, Leuven, Belgium) (left figure in Fig. 1) was used for phantom validation. Three different deformations of this phantom were first scanned by CT to gain the ground truth of these deformations. Each deformation was then viewed by X-ray fluoroscopy from different viewing directions. Both CT and X-ray fluoroscopy were obtained by a GE C-arm system. We collected X-ray images from five different viewing angles with Positioner Primary Angle $\{-30°, -15°, 0°, 15°, 30°\}$ and Positioner Secondary Angle $0°$ [2]. The aortic exterior surface was segmented from CT-scan by ITK-SNAP [26] and pre-processed by MeshLab [27] to obtain the triangular surface mesh representing the aortic model of each deformation. For each phantom experiment, a mesh from CT was used as the pre-operative model. The X-ray images and CT of another deformation were used as the intra-operative observations and ground truth, respectively. The registration between CT and X-ray fluoroscopy was performed using ICP.

2) Simulation setup: Using one of the aortic mesh segmented from CT as the pre-operative model, simulations with three datasets were conducted (Fig. 5). The deformations from pre-operative model to intra-operative model were performed by ED graph (green colour in Fig. 5). The feature pixels from different viewing directions were then simulated by first projecting the ground truth from these directions using (1) and then calculating the edge of the projected point cloud using alpha-shape [22]. In these simulations, we treated y-axis in Fig. 5 as the rotation axis of Positioner Primary Angle. For each dataset, we generated five observations by setting Positioner Primary Angle as $\{-30°, -15°, 0°, 15°, 30°\}$.

3) Parameter setup: The parameters of the proposed reconstruction framework were chosen empirically. In all simulations and experiments, we chose $\theta_{\text{th}} = \frac{\pi}{6}$ (rad), $d_{\text{th}} = 30$ (pixels) for registration, and $w_{\text{rot}} = 1$, $w_{\text{reg}} = 1$, $w_{\text{ob}} = 1$

[2] These angles represent the rotation degrees of the X-Ray image intensifier. Please refer to DICOM attributes for more information.

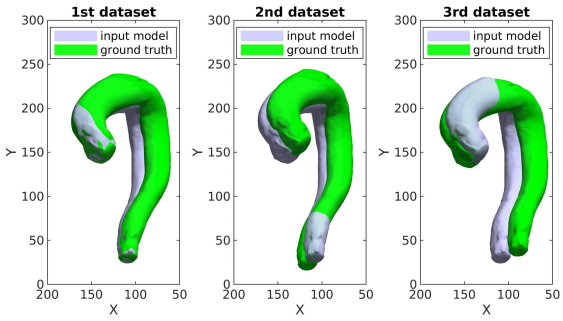

Fig. 5. Datasets for simulations. Grey: pre-operative model, green: ground truth of intra-operative model, unit mm. For each dataset, intra-operative images were simulated from five different directions.

for optimization. The number of nearest ED nodes K in (4) was set as 15. For better smoothing performance, the number of neighbouring nodes in (7) was set as half of the total number of ED nodes.

B. Metrics for error measurement

We used point to plane distance to measure the error between the 3D reconstruction result and the ground truth. Suppose $\hat{\mathbf{P}}$ denotes the estimated 3D position of a vertex and $\mathbf{P}^{\text{gt}} \in \mathbb{R}^3$ denotes the position of its corresponding vertex from ground truth. The reconstruction error of $\hat{\mathbf{P}}$ is:

$$e_i = \text{abs}\left(\tilde{\mathbf{n}}(\mathbf{P}^{\text{gt}})^\top(\hat{\mathbf{P}} - \mathbf{P}^{\text{gt}})\right), \tag{10}$$

where $\tilde{\mathbf{n}}(\cdot) \in \mathbb{R}^3$ denotes the 3D normal vector of a vertex.

C. Accuracy and robustness assessment

1) Accuracy assessment: Using observation without noise, the first simulation assessed the accuracy of reconstruction result under perfect condition. Fig. 6 shows the reconstruction accuracy when using different numbers of intra-operative observations. To show the necessity of using at least two images, we present the result of using one image by fixing the depth of a vertex from the pre-operative model. Fig. 6 shows that the reconstruction accuracy significantly increases when using more than one images.

By comparing the reconstruction result in Fig. 6, we can see that from two to five images, the reconstruction accuracy is similar. This illustrates that two intra-operative images are enough for the proposed framework to recover aortic deformation. Under the perfect condition, this framework can recover aortic shape with reconstruction error around 0.7mm-0.8mm when using only two intra-operative images.

2) Robustness assessment: In practice, observations are corrupted by noises. To evaluate the robustness of the proposed framework when using noisy observations, we conducted Monte Carlo simulations with 500 independent runs under different noise levels. We used the same datasets with two intra-operative observations as in the previous simulation. Zero mean Gaussian noises with standard deviations $\{0.2, 0.5, 1.0, 1.5, 2.0, 2.5, 3.0\}$ (pixels) were added to the features from each observation. Table I shows the average reconstruction error of each Monte Carlo simulation. For all datasets, when the noise level is small, reconstruction accuracy is close to the original result of using perfect observations. Besides, when the noise level increases 1500% from 0.2 to 3.0 (pixels), the reconstruction error increases only 53.2%, 27.8%, and 76.7% for the three datasets, respectively. The two main reasons of this robustness are: i) the proposed registration approach is able to provide robust correspondence; ii) the regularization term (7) designed for smoothing the deformation also contributes to the robustness for noisy observation.

TABLE I

RECONSTRUCTION ERROR WITH/WITHOUT OBSERVATION NOISES

Data	Org.	Monte Carlo of different noise level						
		0.2	0.5	1.0	1.5	2.0	2.5	3.0
1st	0.812	0.832	0.836	0.847	0.853	0.906	1.040	1.275
2nd	0.681	0.693	0.694	0.695	0.695	0.701	0.741	0.886
3rd	0.702	0.712	0.713	0.716	0.730	0.784	0.969	1.258

Org.: reconstruction error (in mm) using two images without noise.
Noise level: standard deviation in pixel.
The average reconstruction error of 500 runs is presented.

D. Phantom experiment

Here we present the phantom results using two intra-operative X-ray images. The viewing directions [3] of three experiments are shown in Table II. The pre-operative model and 3D reconstruction result are shown in Fig. 7. The error figures (the third column in Fig. 7) demonstrate that most parts of the aorta have been recovered with low error (blue). From the fourth column in Fig. 7 and Table II we see that the reconstruction error is around 0.9mm-1.2mm.

TABLE II

VIEWING DIRECTIONS & RECONSTRUCTION ACCURACY OF PHANTOMS

Data	Img. 1	Img. 2	3D init.	3D err.	3D imp.%	2D err.	2D imp.%
1st	AP	LAO 30	6.464	0.870	86.5%	0.292	97.3%
2nd	LAO 15	RAO 15	9.033	0.881	90.2%	0.374	97.4%
3rd	AP	LAO 30	5.873	1.226	79.1%	0.405	94.0%

Img. 1/2: the viewing directions of the two images in Fig. 7.
3D init.: initial difference (in mm) between pre-operative model and ground truth.
3D err.: absolute error (in mm) of 3D reconstruction result.
2D err.: absolute error (in mm) of reprojection.
3D imp.%: the 3D accuracy improvement by $\frac{\text{initial error} - \text{result error}}{\text{initial error}}$.
2D imp.%: the 2D reprojection improvement.

In the third experiment, we present the reconstruction result using fluoroscopy with large occlusions (bottom right in Fig. 7). For real MIS, we can wisely view the aorta from the directions with fewer occlusions on fluoroscopy, e.g. the second experiment.

The last two columns in Fig. 7 present the intra-operative images, the projection of aortic wall contour from the pre-operative model (blue), and the 3D reconstruction of aortic wall contour reprojected on the fluoroscopy (red). We can see that the reprojections are almost the same as the observations from fluoroscopy. The 2D reprojection error is around 0.3mm-0.4mm, which decreases over 90% from the initial error for all experiments (Table II).

[3] LAO, RAO, and AP: $+$, $-$, and 0° of Positioner Primary Angle. Please refer to DICOM attributes for more information.

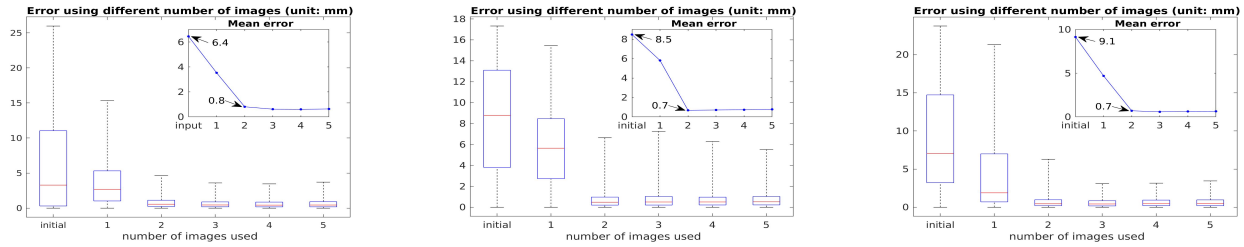

(a) Reconstruction error of the 1st dataset (b) Reconstruction error of the 2nd dataset (c) Reconstruction error of the 3rd dataset

Fig. 6. Reconstruction error using observations from different directions. The corresponding datasets are shown in Fig. 5. The reconstruction error (in mm) was calculated by (10). The small figures on top right corner present the mean reconstruction error. More details are described in Section IV-C.1.

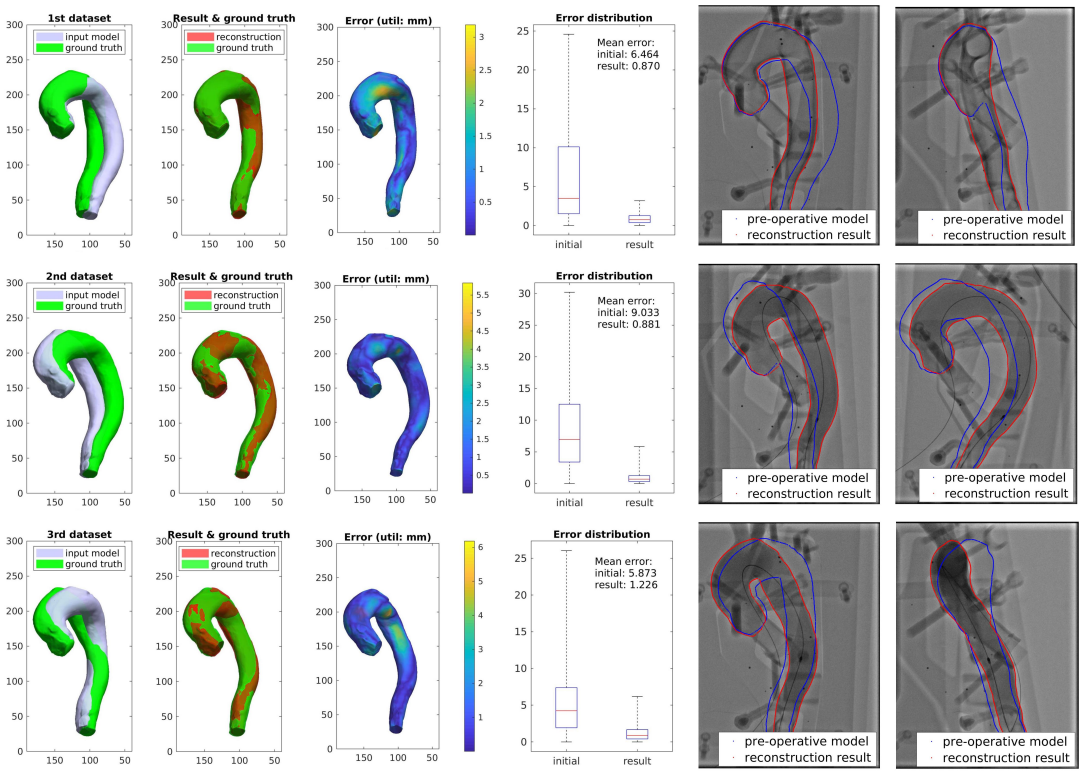

Fig. 7. Reconstruction of phantom experiments using two intra-operative images. Each row represents the data and result of different experiments. The 1st column shows the input pre-operative model (grey) and the ground truth of intra-operative model (green). The 2nd column shows the reconstruction result (red) and the ground truth (green). The 3rd column shows the reconstruction error of each vertex, where blue parts denotes low reconstruction error. The 4th column shows the error distribution of input the pre-operative model and the reconstruction result. The last two columns show the two images. The projection of vessel wall contours of pre-operative model (blue) and the reprejection of reconstruction result (red) are also presented. The red curves illustrates that, for all experiments, the reprojections of reconstructed aortic wall contour are almost the same as the observations from fluoroscopy.

V. Conclusion

This paper presents a robust framework that recovers aortic 3D shape intra-operatively using multiple X-ray fluoroscopy from different viewing directions. Different from some existing deformation reconstruction frameworks, the proposed reconstruction framework uses pixels presenting aortic wall contours as the observed features due to the limitation of orthographic projection and the occluded areas on X-ray fluoroscopy. The corresponding 3D vertices from the pre-operative model are calculated via a 2D-3D non-rigid registration approach, and the vessel's reconstruction is formulated as a nonlinear least squares problem based on embedded deformation graph. Detailed validation by simulation and phantom experiments is conducted. The result demonstrates the accuracy and robustness of the proposed framework, as well as its ability to reconstruct aortic 3D shape with only two intra-operative X-ray images from different directions. This illustrates the potential clinical value of this framework to be used for G-arm or biplane angiography system.

Current framework does not consider the feature extraction procedure. In the future, we plan to add this front-end using deep learning approaches, e.g. [28]. We will further investigate the effect of the registration on the quality of reconstruction. Besides, we plan to improve the registration process for increasing the calculation speed. The proposed framework is currently implemented using Matlab. Our final goal is a real-time aorta reconstruction system based on the proposed method.

REFERENCES

[1] J. May, G. White, R. Waugh, P. Petrasek, X. Chaufour, M. Arulchelvam, M. Stephen, and J. Harris, "Life-table analysis of primary and assisted success following endoluminal repair of abdominal aortic aneurysms: the role of supplementary endovascular intervention in improving outcome," *European Journal of Vascular and Endovascular Surgery*, vol. 19, no. 6, pp. 648–655, 2000.

[2] B. Funaki, "Endovascular intervention for the treatment of acute arterial gastrointestinal hemorrhage," *Gastroenterology Clinics*, vol. 31, no. 3, pp. 701–713, 2002.

[3] A. Vahanian, O. R. Alfieri, N. Al-Attar, M. J. Antunes, J. Bax, B. Cormier, A. Cribier, P. De Jaegere, G. Fournial, A. P. Kappetein, *et al.*, "Transcatheter valve implantation for patients with aortic stenosis: a position statement from the european association of cardio-thoracic surgery (eacts) and the european society of cardiology (esc), in collaboration with the european association of percutaneous cardiovascular interventions (eapci)," *European Journal of Cardio-Thoracic Surgery*, vol. 34, no. 1, pp. 1–8, 2008.

[4] T. Walther, M. W. Chu, and F. W. Mohr, "Transcatheter aortic valve implantation: time to expand?" *Current opinion in cardiology*, vol. 23, no. 2, pp. 111–116, 2008.

[5] T. Walther, V. Falk, J. Kempfert, M. A. Borger, J. Fassl, M. W. Chu, G. Schuler, and F. W. Mohr, "Transapical minimally invasive aortic valve implantation; the initial 50 patients," *European Journal of Cardio-Thoracic Surgery*, vol. 33, no. 6, pp. 983–988, 2008.

[6] R. Zahn, R. Schiele, C. Kilkowski, B. Klein, U. Zeymer, C. Werling, A. Lehmann, U. Gerckens, and W. Saggau, "Correction of aortic regurgitation after transcatheter aortic valve implantation of the medtronic corevalvetm prosthesis due to a too-low implantation, using transcatheter repositioning." *The Journal of heart valve disease*, vol. 20, no. 1, pp. 64–69, 2011.

[7] M. J. Davidson, J. K. White, and D. S. Baim, "Percutaneous therapies for valvular heart disease," *Cardiovascular pathology*, vol. 15, no. 3, pp. 123–129, 2006.

[8] J. Burgner, S. D. Herrell, and R. J. Webster, "Toward fluoroscopic shape reconstruction for control of steerable medical devices," in *ASME 2011 Dynamic Systems and Control Conference and Bath/ASME Symposium on Fluid Power and Motion Control*. American Society of Mechanical Engineers, 2011, pp. 791–794.

[9] L. Zhao, S. Giannarou, S.-L. Lee, and G.-Z. Yang, "Scem+: real-time robust simultaneous catheter and environment modeling for endovascular navigation," *IEEE Robotics and Automation Letters*, vol. 1, no. 2, pp. 961–968, 2016.

[10] G. Zheng, M. A. Ballester, M. Styner, and L.-P. Nolte, "Reconstruction of patient-specific 3d bone surface from 2d calibrated fluoroscopic images and point distribution model," in *International Conference on Medical Image Computing and Computer-Assisted Intervention*. Springer, 2006, pp. 25–32.

[11] G. Zheng, S. Gollmer, S. Schumann, X. Dong, T. Feilkas, and M. A. G. Ballester, "A 2d/3d correspondence building method for reconstruction of a patient-specific 3d bone surface model using point distribution models and calibrated x-ray images," *Medical Image Analysis*, vol. 13, no. 6, pp. 883–899, 2009.

[12] N. Baka, B. L. Kaptein, M. de Bruijne, T. van Walsum, J. Giphart, W. J. Niessen, and B. P. Lelieveldt, "2d–3d shape reconstruction of the distal femur from stereo x-ray imaging using statistical shape models," *Medical image analysis*, vol. 15, no. 6, pp. 840–850, 2011.

[13] D. Toth, M. Pfister, A. Maier, M. Kowarschik, and J. Hornegger, "Adaption of 3d models to 2d x-ray images during endovascular abdominal aneurysm repair," in *International Conference on Medical Image Computing and Computer-Assisted Intervention*. Springer, 2015, pp. 339–346.

[14] R. A. Newcombe, D. Fox, and S. M. Seitz, "Dynamicfusion: Reconstruction and tracking of non-rigid scenes in real-time," in *Proceedings of the IEEE conference on computer vision and pattern recognition*, 2015, pp. 343–352.

[15] R. A. Newcombe, S. Izadi, O. Hilliges, D. Molyneaux, D. Kim, A. J. Davison, P. Kohli, J. Shotton, S. Hodges, and A. W. Fitzgibbon, "Kinectfusion: Real-time dense surface mapping and tracking." in *International Symposium on Mixed and Augmented Reality*, 2011, pp. 127–136.

[16] L. Kavan, S. Collins, J. Žára, and C. O'Sullivan, "Skinning with dual quaternions," in *Proceedings of the 2007 symposium on Interactive 3D graphics and games*. ACM, 2007, pp. 39–46.

[17] M. Innmann, M. Zollhöfer, M. Nießner, C. Theobalt, and M. Stamminger, "Volumedeform: Real-time volumetric non-rigid reconstruction," in *European Conference on Computer Vision*. Springer, 2016, pp. 362–379.

[18] M. Dou, S. Khamis, Y. Degtyarev, P. Davidson, S. R. Fanello, A. Kowdle, S. O. Escolano, C. Rhemann, D. Kim, J. Taylor, *et al.*, "Fusion4d: Real-time performance capture of challenging scenes," *ACM Transactions on Graphics (TOG)*, vol. 35, no. 4, p. 114, 2016.

[19] W. Gao and R. Tedrake, "Surfelwarp: Efficient non-volumetric single view dynamic reconstruction," in *Robotics: Science and System (RSS)*, 2018.

[20] J. Song, J. Wang, L. Zhao, S. Huang, and G. Dissanayake, "Mis-slam: Real-time large-scale dense deformable slam system in minimal invasive surgery based on heterogeneous computing," *IEEE Robotics and Automation Letters*, vol. 3, no. 4, pp. 4068–4075, 2018.

[21] R. W. Sumner, J. Schmid, and M. Pauly, "Embedded deformation for shape manipulation," *ACM Transactions on Graphics (TOG)*, vol. 26, no. 3, p. 80, 2007.

[22] H. Edelsbrunner, D. Kirkpatrick, and R. Seidel, "On the shape of a set of points in the plane," *IEEE Transactions on information theory*, vol. 29, no. 4, pp. 551–559, 1983.

[23] P. J. Besl and N. D. McKay, "A method for registration of 3-d shapes," in *Sensor Fusion IV: Control Paradigms and Data Structures*, vol. 1611. International Society for Optics and Photonics, 1992, pp. 586–607.

[24] J. Song, J. Wang, L. Zhao, S. Huang, and G. Dissanayake, "Dynamic reconstruction of deformable soft-tissue with stereo scope in minimal invasive surgery," *IEEE Robotics and Automation Letters*, vol. 3, no. 1, pp. 155–162, 2018.

[25] J. Nocedal and S. Wright, *Numerical optimization*. Springer Science & Business Media, 2006.

[26] P. A. Yushkevich, J. Piven, H. Cody Hazlett, R. Gimpel Smith, S. Ho, J. C. Gee, and G. Gerig, "User-guided 3D active contour segmentation of anatomical structures: Significantly improved efficiency and reliability," *Neuroimage*, vol. 31, no. 3, pp. 1116–1128, 2006.

[27] P. Cignoni, M. Callieri, M. Corsini, M. Dellepiane, F. Ganovelli, and G. Ranzuglia, "Meshlab: an open-source mesh processing tool." in *Eurographics Italian chapter conference*, 2008, pp. 129–136.

[28] O. Ronneberger, P. Fischer, and T. Brox, "U-net: Convolutional networks for biomedical image segmentation," in *International Conference on Medical image computing and computer-assisted intervention*. Springer, 2015, pp. 234–241.